A study of rheological limitations in rotary jet spinning of polymer nanofibers through modeling and experimentation

Rogalski, James J.; Botto, Lorenzo; Bastiaansen, Cees W.M.; Peijs, Ton

Important note
To cite this publication, please use the final published version (if applicable).
Please check the document version above.

JOURNAL OF Applied Polymer SCIENCE

A study of rheological limitations in rotary jet spinning of polymer nanofibers through modeling and experimentation

James J. Rogalski,[1] Lorenzo Botto,[1,2] Cees W. M. Bastiaansen,[1,3] Ton Peijs [ORCID][4]

[1]School of Engineering and Materials Science, Queen Mary University of London, Mile End Road, London E1 4NS, UK
[2]Process & Energy Department, 3ME Faculty, TU Delft, 2628 CB, Delft, The Netherlands
[3]Faculty of Chemistry and Chemical Engineering, Eindhoven University of Technology, P.O. Box 513, 5600 MB, Eindhoven, The Netherlands
[4]Materials Engineering Centre, WMG, University of Warwick, Coventry CV4 7AL, UK
Correspondence to: T. Peijs (E-mail: t.peijs@warwick.ac.uk)

ABSTRACT: The recently popularized method of rotary jet spinning (RJS) or centrifugal spinning is investigated to evaluate the rheological limitations of polymer solutions and melts to optimal spinnability. The influence of Newtonian or non-Newtonian behavior of the polymer on spinnability is discussed. We observe that highly viscous polymers tend to block the die channels within a rotary jet spinneret and therefore suggest the use of relatively low Newtonian viscosities of between 1 and 10 Pa s for optimal fiber production. Computational fluid dynamics simulations are used in conjunction with experimental data to establish important processing parameters, such as typical shear rates in the device and optimal polymer melt or solution viscosities. A theoretical model for RJS is compared to measured fiber diameters. The comparison shows that although fiber diameters can be estimated very roughly in the case of polymer solutions, the prediction of fiber diameter in the case of polymer melts require further modeling work. © 2020 Wiley Periodicals, Inc. J. Appl. Polym. Sci. **2020**, *137*, 48963.

INTRODUCTION

The production of polymeric nanofibers is a growing research field since the early work of D. H. Reneker in the 1990s.[1] Applications ranging from drug delivery, wound dressing, filtration, sensors, composites, and battery separators[2] call for production techniques characterized by low cost and high production rates.

A recent nanofiber production technique, rotary jet spinning (RJS), also known as centrifugal spinning or Forcespinning, has gained in popularity since around 2010 by promising higher production rates and economies of scale in comparison to methods such as electrospinning (ES)[3–5] and melt blowing.[6–8] Other methods such as islands in the sea spinning,[9,10] template synthesis,[11–13] drawing,[14] phase-separation,[15] and self-assembly[16,17] are all less suitable for large-scale production. RJS offers the benefits of low power consumption, submicron fiber diameters, and high production rates. Reported maximum production rates are 1500 g h^{-1} for melt blowing[18] and 200 g h^{-1} for needle-less ES.[19] In contrast, industrial scale RJS setups such as the Fiberio FX2200 achieves around 12,000 g h^{-1},[2] making RJS of great interest to industry. RJS allows the production of fibers from either a polymer solution or melt. However, not much is known about which type of materials can be used with this method nor about the operational parameters that produce fibers.

The RJS process works by using a rotating vessel which is lined with two or more orifices around its axis of rotation. At a sufficiently large rotational velocity, the centrifugal force ejects the polymer, which is subsequently drawn into a thin fiber due to the continuously moving die and stationary collector. The fiber undergoes solidification by solvent evaporation (solutions) or rapid cooling (melt) before being collected at a set distance using one of multiple collection methods.[2]

Only a handful of polymers such as poly(butylene terephthalate) (PBT),[20] polypropylene (PP),[21–23] polycaprolactone (PCL),[24] and poly(ethylene terephthalate) (PET)[25] have been reported to date for RJS of polymer melts,. Polymer solutions are more widely studied in RJS, with fibers being successfully spun from polyamide 6 (PA6),[26] poly(ethylene oxide) (PEO),[27,28] PCL,[29] poly(L-lactic acid) (PLLA),[30] and polyacrylonitrile (PAN)[31] solutions. RJS requires a suitable range of fluid viscosity values for a fiber to form. It is this range that we seek to quantify in this study. Polymer solution viscosities can be altered by changing the polymer weight fraction and molecular weight. Polymer melt viscosities can be varied by changing molecular weight and temperature.

In solution RJS, the dependence of the polymer weight percentage has been investigated by Ren *et al.*,[30] who identified three

viscosity regimes (Figure 1, left). At a critical polymer concentration $C*$ polymer chain entanglement occurs, resulting in a sudden increase in the zero-shear viscosity which is captured by the Rouse-Zimm model.[32,33] The critical concentration can be estimated using the following equation[34]:

$$C* = \frac{M_w}{R_g^3 N_A} \qquad (1)$$

where M_w is the weight average molecular weight, R_g is the radius of gyration, and N_A is Avogadro's constant.

Ren et al. reported critical concentrations for PLLA/PVP (polyvinylpyrrolidone) in dichloromethane solutions ranging from 1 to 10 wt % (for PLLA/PVP ratios in the range 10–100% PLLA); a concentration of 8 wt % was reported for the formation of the first nonbeaded fibers by RJS. A study by Lu et al.[35] evaluated the rotary jet spinnability of fibers from solutions of PAN (M_w = 150,000) and N,N-dimethyl-formamide. They also concluded that bead free fibers could be produced from concentrations starting at 10 wt %.

Regarding polymer melts, two rheological processing regimes are relevant (Figure 1, right). These regimes, characterized by different dependency of viscosity on the degree of chain entanglements, are separated by the so-called entanglement molecular weight (M_e). Before M_e, the slope of the $\eta_0 - M_w$ curve in logarithmic scale is ~1, whereas for molecular weights larger than M_e the slope increases to ~3.4, suggesting

$$\eta_0 \propto M_w^{3.4} \qquad (2)$$

Typical entanglement molecular weights for polymers, as calculated by Vega et al., include polyethylene (PE) at 1200 g mol^{-1}, PP at 5200 g mol^{-1}, and polystyrene at 14,900 g mol^{-1}.[36] Molecular weight is not the only variable affecting viscosity. According to Yan et al.,[37] the viscoelastic properties of PE's are strongly affected by the branching of the polymer chains. These authors observed that compared to their linear counterparts with the same molecular weights, branched PE's gave higher viscosities at lower shear rates and lower viscosities at high shear rates. A similar study by Vega et al.[38] into the rheological behavior of 13 narrow molecular weight distribution long chain branched (LCB) PE's resulted in eight of the polymers exhibiting different rheological behaviors to that expected from linear (non-LCB) polyethylene's.

The rheological behavior below $C*$ and M_e is approximately Newtonian. For larger concentrations or molecular weights, the viscosity depends on the shear rate. Furthermore, in the dense regime, the extensional viscosity could be important.

Previous works attempting to quantify the regimes of RJS fiber production have yielded limited information on the range of materials that can produce fibers for a given set of operational parameters. Studies to date include a simple model for fiber size estimation from Mellado et al.[39] and several models for trends in fiber diameter and trajectories,[40–43] including models comparing Newtonian and non-Newtonian viscoelastic flow behavior.[44] These studies have exclusively analyzed fiber characteristics, such as trajectory and regions of fiber size reduction within the trajectory arc; however, they have not discussed the effect of changing rheological properties and their effect on spinnability (these studies invariably assumed that the polymer will produce a fiber, while this in practice is often not the case). In this article, this knowledge gap is addressed. Experiments are carried out to quantify the regime of operational and rheological parameters for which fibers form in a RJS device, using both polymer solutions and polymer melts. We carried out rheological experiments on these fluids, to quantify the dependence of the viscosity on the shear rate and on the polymer concentration (for solutions) or molecular weight (for melts). The physical experiments are complemented with a basic computational fluid dynamics (CFD) analysis, which is used to illustrate certain features of the polymer flow within the device and quantify characteristic values of the shear rate occurring during device operation.

To determine the spinnability of selected polymers for both solution and melt, physical experimentation and CFD simulations were performed. Physical testing was conducted using a Fiberio L-1000D (USA) rotary jet spinner, whereas CFD was conducted using ANSYS CFX software. Solution spinning was the primary focus for the CFD analysis; however, both solution and melt spinning experiments were conducted in the physical spinning trials.
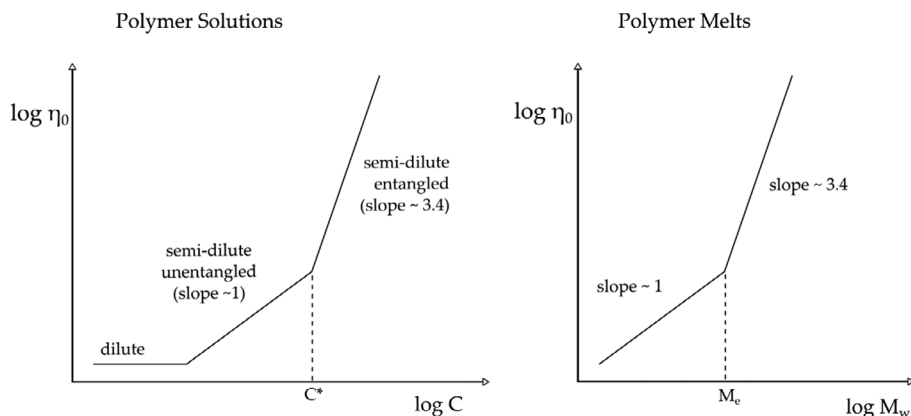
Figure 1. Schematic showing the change in viscosity in polymer solutions (left) past the critical concentration. Polymer melts (right) have a similar critical molecular weight (M_e) at which sufficient chain entanglement occurs.

MATERIALS

The polymeric materials chosen for melt and solution spinning are presented in Tables I and II, respectively. A selection of PE's was used with varying molecular weights for the melt spinning experiments (Table I), while PA6–formic acid solutions were created with different polymer concentrations in solution with the aid of magnetic stirrers for solution spinning experiments (Table II).

All polymers used were dried at 80 °C for a period of 24 h as per the manufacturer recommendations prior to use in melt spinning and solution mixing to remove any residual moisture. After combining polymer and solvent, all solutions were stirred for several hours to ensure complete homogeneity before characterization and fiber spinning, which occurred immediately afterward.

RESULTS

Rheology

For spinning processes, the extensional viscosity is an important parameter. However, measurements of extensional viscosity are challenging and require specialized equipment. Therefore, we have resorted to measuring shear viscosity only, under the hypothesis that the shear viscosity is proportional to the extensional viscosity for polymeric liquids that behave approximately Newtonian (for pure Newtonian fluids the Trouton ratio—being the ratio of extensional viscosity to shear viscosity—is 3). However, also outside the Newtonian regime, the characterization of shear viscosity still provides useful information about the response of a solution or melt to deformation.

Measurements of shear viscosity were obtained using both a TA Instruments AR2000 (for melts) and TA Instruments DHR3 (for solutions). Measurements were carried out in a plate-plate configuration, with solutions being characterized at 23 °C immediately following several hours of stirring to reduce the effect of polymer degradation from solvent. Shear viscosity versus shear rate curves for solutions and melts are shown in Figures 2 and 3, and are tabulated in Table III. For polymers that exhibit non-Newtonian flow behavior, rheological models were fitted to the flow curves for further analysis. The non-Newtonian model that showed the best fit for the measured data was the Cross model[45]:

$$\frac{\eta - \eta_\infty}{\eta_0 - \eta_\infty} = \frac{1}{1 + (k\dot{\gamma})^n} \tag{3}$$

where η_0 represents the zero-shear viscosity, η_∞ represents the constant apparent viscosity attained at high shear rates, k is a time constant, $\dot{\gamma}$ is the shear rate, and n is the power law index.

Table II. Polymer Solutions Used in Rotary Jet Solution Spinning Trials

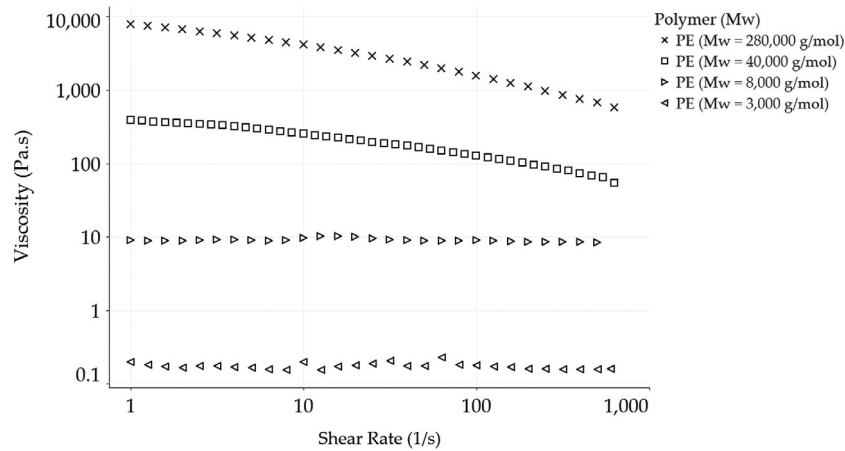| Ref.	Polymer	Solvent	Polymer wt %
5–11	Polyamide 6 (Durethan B31F, Lanxess)	Formic Acid	1, 5, 10, 15, 20, 25, 30

Computational Fluid Dynamics

To complement the experimental results, we carried out a series of CFD simulations. The relevant portion of the channel geometry adopted in the simulations is identical to that of the rotary jet spinner. The controlling flow parameters (e.g., inlet pressure) in the simulation were chosen to match the operating parameters in the experiments (e.g., rotational velocity).

In this article, these CFD simulations serve two main purposes: (1) to illustrate, from a qualitative point of view, the characteristics of the flow within the device, such as the jump in velocity and shear rate corresponding to contractions; (2) to provide a quantification of the maximum shear rates for a given value of the rotational velocity and geometric parameters. This last point is particularly important, because the flowability of the polymer is dependent on the viscosity, and the viscosity changes over a range of applied shear rates that only the simulations enable to estimate, although crudely. We emphasize that, given that local flow variables are not measured in our experiments, the simulations complement the experimental data rather than being validated by the experiments.

The geometrical and operating variables used in the CFD simulations were identical to the experimental ones. The internal geometry of the spinneret was replicated exactly in the CFD simulation, starting from a CAD model of the full device [Figure 4(a–c)]. The rotational velocity in each simulation was varied between 5000 and 12,000 rpm, in steps of 1000 rpm. To explore a reasonably large parameter space, we carried out 56 simulations for different combinations of viscosities and rotational velocities.

Each simulation assumed a constant viscosity η. This parameter was varied between 1 and 30 Pa s in steps of 5 Pa s. While the polymer melts and solutions employed are, strictly speaking, non-Newtonian, the fluid behaves approximately as a Newtonian fluid for η less than about 10 Pa s. For more viscous polymer melts, the dependence of η on the shear rate is marked. However, assuming a constant η still provides an illustration of the flow distribution and a rough estimate of the typical shear rate values.

To drive the flow, we imposed an inlet pressure corresponding to the assigned rotational velocity [using eq. (4), which will be described

Table I. Polymers Used in Rotary Jet Melt Spinning Trials

Ref.	Polymer	M_w (g mol^{-1})	Polydispersity index	T_m (°C)
1	Polyethylene (Polywax 3000, Baker Hughes)	3000	~1.08	129
2	Polyethylene (HI-WAX, Mitsui Chemicals)	8000	~1.08	129
3	Polyethylene (Riblene MT10R, Versalis S.p.A.)	40,000	Unavailable	106
4	Polyethylene (InnoPlus HD5000S, PTT Chemical)	280,000	Unavailable	125

Figure 2. Viscosity measurements from plate-plate rheometry for polymer melts used in RJS, showing a change from Newtonian behavior for low M_w polyethylene to the non-Newtonian shear thinning behavior for higher M_w polyethylene's.
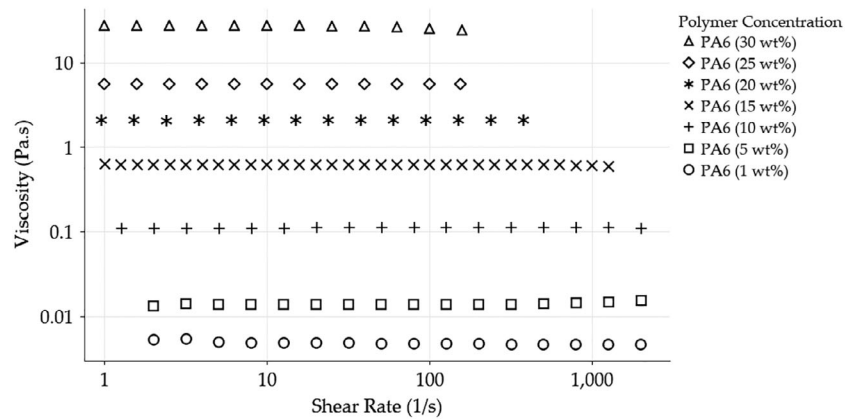

Figure 3. Viscosity measurements from plate-plate rheometry, showing the flow behavior of the polymer solutions used in RJS. All PA6 solutions in formic acid exhibited Newtonian behavior throughout all concentrations.

Table III. Viscosity Data for the Range of Polymer Solutions and Melts Evaluated in RJS

Ref.	Polymer	Model	η_0 (Pa s)	η_∞ (Pa s)	k (s)	n
1	PE—M_w 3000 g mol^{-1}	Newtonian	0.145	-	-	-
2	PE—M_w 8000 g mol^{-1}	Newtonian	8.58	-	-	-
3	PE—M_w 40,000 g mol^{-1}	Cross	453	3	0.095	0.48
4	PE—M_w 280,000 g mol^{-1}	Cross	13 156	254	0.653	0.455
5	PA6—1 wt %	Newtonian	0.005	-	-	-
6	PA6—5 wt %	Newtonian	0.015	-	-	-
7	PA6—10 wt %	Newtonian	0.111	-	-	-
8	PA6—15 wt %	Newtonian	0.598	-	-	-
9	PA6—20 wt %	Newtonian	2.09	-	-	-
10	PA6—25 wt %	Newtonian	5.58	-	-	-
11	PA6—30 wt %	Newtonian	25.9	-	-	-

Newtonian flow behavior parameters are shown as well as Cross-model parameters for the non-Newtonian systems.
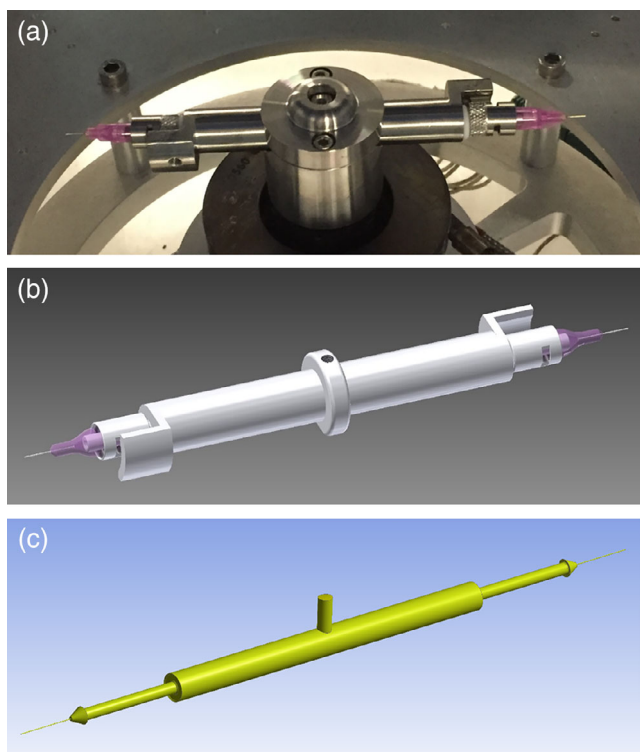
Figure 4. Rotary jet spinneret geometry from (a) the Fiberio L1000-D equipment and (b) its CAD representation; (c) the internal geometry used in the CFD simulations. [Color figure can be viewed at wileyonlinelibrary.com]

later, to map pressure and velocity] and enforce atmospheric pressure at the outlet. The fluid was assumed not to slip at the walls. All the simulations were run at steady state.

The spatial distribution of maximum flow velocity and shear rate in different parts of the device is shown for η = 1 Pa s and 10,000 rpm in Figure 5. The pressure distribution corresponding to η = 10 Pa s and 10,000 rpm is shown in Figure 6. The feature most relevant to the interpretation of the experiments is that the geometrical constriction going from the spinneret to the needle causes the flow velocity to increase at the constriction by more than five orders of magnitude with respect to the upstream value. Correspondingly, the shear rate reaches very high values in the needle, of the order of 10^4 s^{-1} for the simulation in Figure 5. This means that the ability of the polymer to flow depends mostly on the geometry of the needle. The largest shear rate occurs, expectedly, at the wall. We expect that, owing to the shear-thinning property of the fluids we employ, the maximum flow velocities in the actual device will be larger than in the simulations, because the viscosity near the wall will be smaller. However, the characteristic order of magnitude of the shear rate predicted by the simulations (which scale like the characteristic velocity divided by the radius of the channel) is expected to be approximately correct. From Figures 2 and 3, we can see that the in the range of shear rates 1–1000 s^{-1}, the dependence of the viscosity on the shear rate is so weak that the viscosity can be considered practically constant. For larger values of η, the shear-rate dependence is stronger, but the typical velocities and shear rates are smaller

(as seen in Figure 7 for η = 10 Pa s and rotation rates 10,000 and 5000 rpm). Considering Figures 2 and 3, we can assume that the simulations are a reasonably accurate model of reality for viscosities up to values of the order of roughly 10 Pa s. As we will see, the experiments show that for viscosities much larger than 10 Pa s, the device does not produce fibers (Figure 9), so the value of the simulations in this range is limited anyway.

RJS Trials

To evaluate the ability of the various polymer solutions and melts to be spun into fibers, RJS was performed using the materials specified in Tables I and II. Polymers intended for melt spinning were used as is in sample quantities of 100 mg per spin, with solution spinning performed with a volume of 1 mL per spin.

RJS experiments were conducted using each solution or melt, with the outcome recorded to produce a graph showing the zones where successful fiber production occurred. A measure of the driving force for fiber production is the pressure exerted on the polymer as it approaches the die constriction. The reduction in the cross-sectional area results in an increase in the shear rate due to the increased flow velocity and reduction in length. A larger shear rate in turn leads to reductions in viscosity at these locations for non-Newtonian flows.

The pressure at the entry to the die was calculated from the CFD simulation to evaluate the rotational velocity and material density required for RJS to produce a fiber. The pressure due to centrifugal forces acting on the die can be calculated from:

$$P = \rho \Omega^2 S_0^2 \tag{4}$$

where ρ is density, Ω is rotational velocity (rad s^{-1}), and S_0 is the distance from the center of rotation to the entry of the die.

The CFD simulations require the prescription of a Newtonian viscosity, which should be representative of the non-Newtonian viscosity evaluated at relevant shear rates. Based upon the data presented in Figure 8, the viscosity of each non-Newtonian polymer was evaluated at typical RJS shear rates between 500 and 800 s^{-1}. For the analysis, an average of these apparent viscosity values was used. The pressure at the die entry [as calculated from eq. (4)] either forces the polymer through the spinneret or results in a blockage, as observed during RJS experimentation and labeled in Figure 9. This effect is either due to insufficient pressure at the die entry or to the polymer being too viscous. By comparing the pressure and viscosity, a direct comparison can be made regardless of the polymer or spinneret geometry.

Figure 9 shows a comparison of die entry pressure and viscosity values from experimental trials using the polymer systems of Tables I and II. For a 0.16 mm internal diameter die, the data suggest a fiber producing zone (shaded green zone) where the viscosity (at shear rates of about 800 s^{-1}) should be between 0.9 and 10 Pa s.

Fiber production as indicated in Figure 9 does not solely rely on the ability of the polymer solution or melt to flow through the die. Fiber production will also rely on polymer solidification, be that through solvent evaporation or cooling of a polymer melt. In the fast-flowing air of the RJS chamber, the rate at which
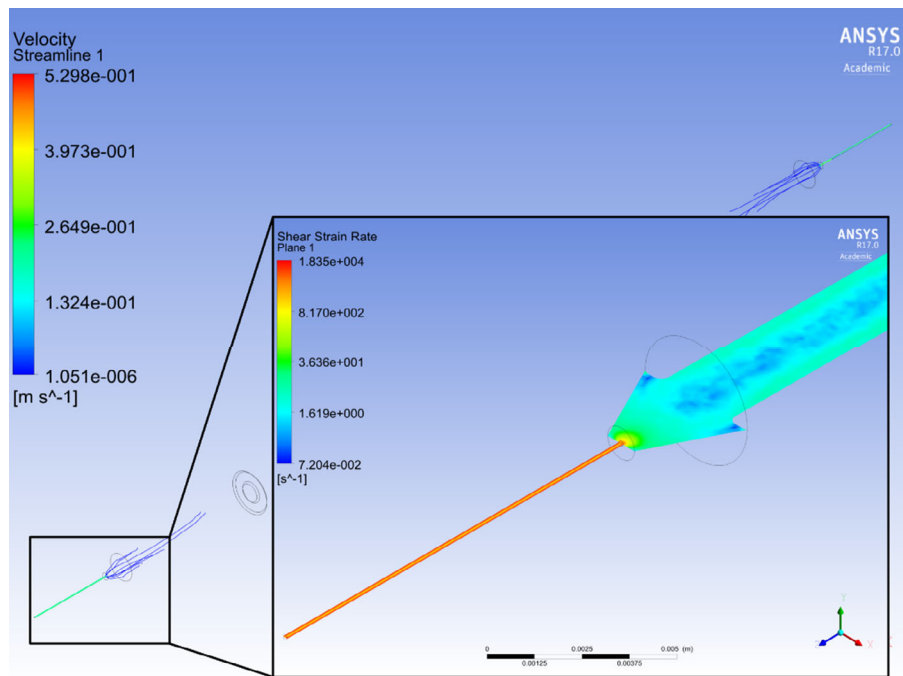
Figure 5. Simulated flow distribution within the spinneret for a viscosity of $\eta = 1$ Pa s and rotation rate of 10,000 rpm (assuming Newtonian fluid). The streamline color scale represents the velocity magnitude. Moving from the spinneret to the needle, the fluid velocity increases from about 10^{-6} to 0.5 m s^{-1}. The inset shows the shear rate distribution. Within the spinneret, the shear rate is highest near the wall, as expected from a Poiseuille flow distribution. [Color figure can be viewed at wileyonlinelibrary.com]

solidification can happen is affected by several factors such as chamber temperature, solvent volatility, solution viscosity, and spinning velocity.[46] Once a fiber has left the spinneret, the fiber is drawn due to the continual motion of the rotating spinneret and the rapid deceleration of the extrudate which is anchored by the continuous connectivity of the fiber to the collector.
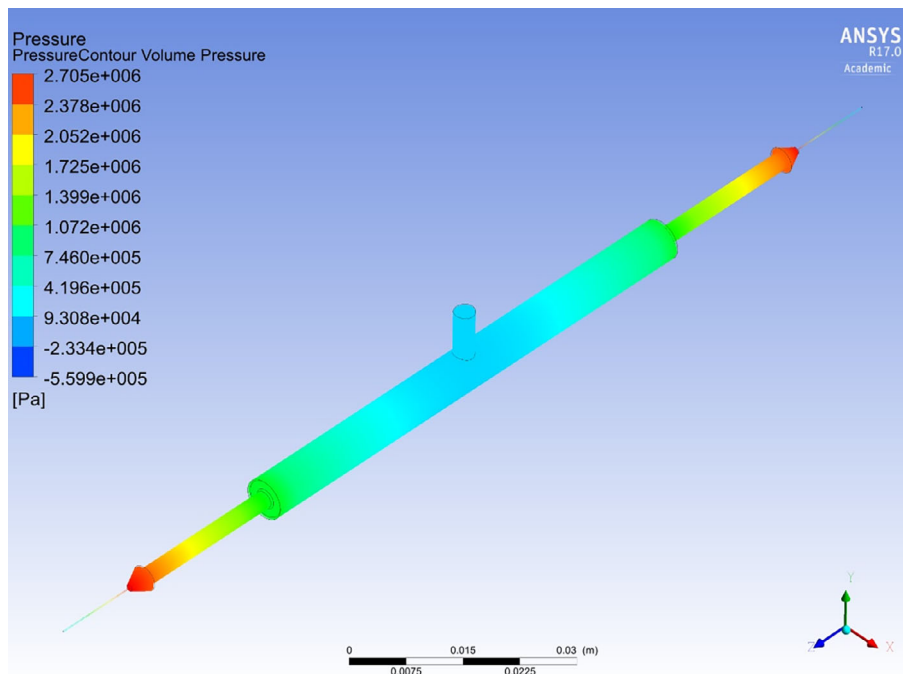
Figure 6. Pressure distribution within the spinneret for $\eta = 10$ Pa s and rotation rate = 10,000 rpm. The pressure is seen to increase approximately linearly from the center of rotation to the entry of the needle. After the fluid has passed this point, the pressure decreases along the die length to reach atmospheric pressure. [Color figure can be viewed at wileyonlinelibrary.com]
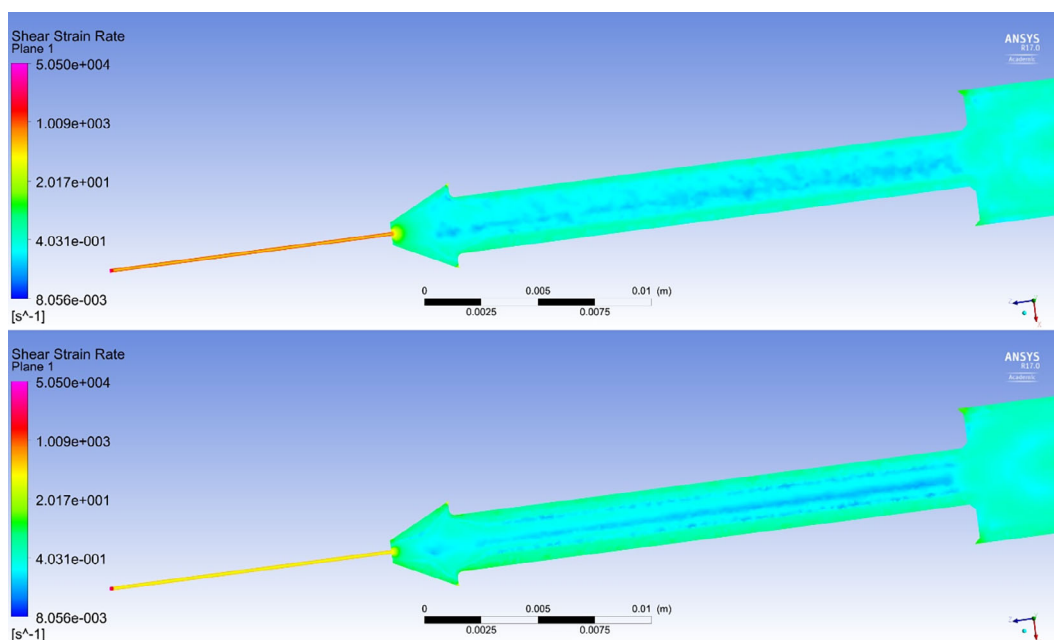
Figure 7. Simulated shear rate distribution for η = 10 Pa s and rotation rates 10,000 rpm (top) and 5000 rpm (bottom). The shear rate magnitude increases due to the higher centrifugal forces produced by the faster rotation. The highest shear rates occur in the region where the polymer exits the die. [Color figure can be viewed at wileyonlinelibrary.com]

Mellado *et al.*[39] produced the following estimate of the fiber radius based on the polymer viscosity and processing parameters:

$$r = \frac{aU^{1/2}\nu^{1/2}}{R_c^{3/2}\Omega}$$ (5)

where a is the diameter of the die (m), U is the velocity of the flow from the die exit (m s^{-1}), ν is the kinematic viscosity $\left(\eta/\rho\right)$, R_c is the collector radius (m), and Ω is the rotational velocity (rad s^{-1}). We have evaluated the ability of eq. (5) to describe our experimental data, focusing on solution spun PA6 fiber diameter data.

In Figure 10, the model by Mellado *et al.* is compared to data on rotary jet spun fibers produced using PA6 solutions only. Our experimental data showed relatively large scatter, and as a result a

Figure 8. Highest shear rates from CFD simulations, using rotational velocities between 5000 and 12,000 rpm. As expected, an increase in shear rates is observed for lower viscosities.
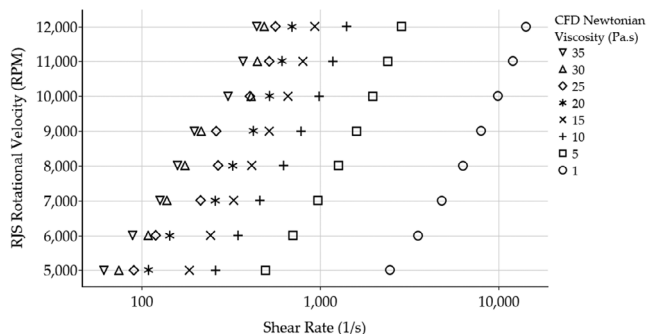
greater than expected variance with respect to model predictions. The model could be improved by considering additional effects such as solvent evaporation. Additional data from solutions containing solvents with higher volatilities and fiber diameters from melt spinning showed even more scatter than Figure 10. For example, diameters for melt spun PE (M_w − 8000 g mol^{-1}) averaged 11 μm, while the model by Mellado *et al.* predicts 1.1 μm.

Although fiber diameters have not been the focus of this study, it is worth noting that fiber diameters produced in a previous study[26] ranged between 350 ± 180 and 500 ± 250 nm when produced from a range of PA6/Formic Acid solutions between 17.5 and 25.0 wt %.

DISCUSSION

In this study, we investigated RJS as a method of fiber production and attempted to discover the lower and upper limits of solution or melt viscosities that would facilitate successful fiber production. The materials chosen for the trials varied in molecular weight and polymer concentration in solution, in the hope that variations in system viscosities and flow behaviors from Newtonian to non-Newtonian would produce differing results, to be analyzed for their impact on fiber spinning.

It was shown that all investigated PA6 solutions showed mostly Newtonian behavior (see Figure 3), while PE's of higher molecular weight exhibited non-Newtonian behavior (see Figure 2). To establish spinnability, experimental trials were performed using each of the polymer systems (see Tables I and II) with varying rotational velocities to establish their potential for fiber production. In addition to experimental data, CFD was performed using a broadly similar range of Newtonian viscosity values.
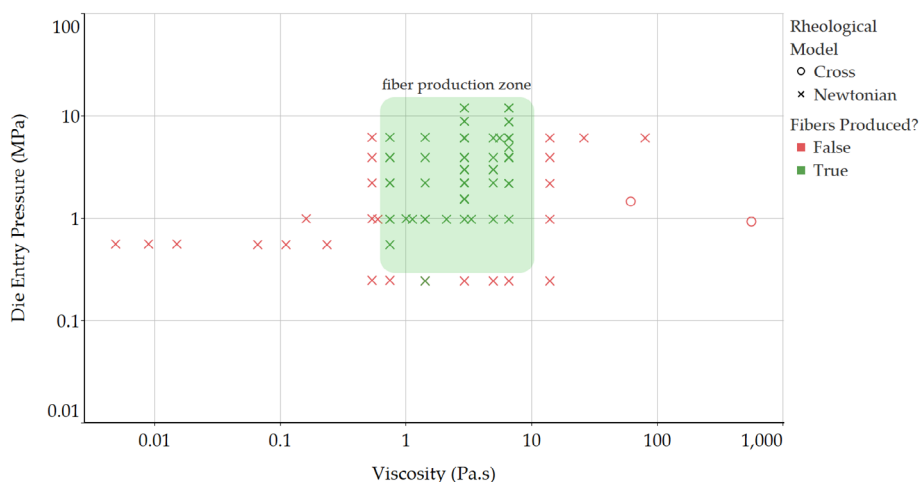
Figure 9. Pressure at the entry of the die versus fluid viscosity. Viscosity is evaluated at shear rate values that correspond to the entrance of the die region. The graph includes data for both fiber producing polymer systems (green symbols within green shaded area) and nonfiber producing polymer systems (red symbols). The green shaded area indicates the range of pressures and viscosities for which a fiber is produced. Too low pressure or too high viscosity will not enable the polymer to flow. [Color figure can be viewed at wileyonlinelibrary.com]

The CFD results demonstrated the flow behavior within the geometry at various rotational velocities. Flow evaluation variables included the flow velocity and shear rates at varying positions within the geometry. Figures 5–7 showed visualizations of the flow behavior. From these images, we can see that at the entry to the die, an area of rapidly increasing flow velocity is present due to a sudden decrease in cross-sectional area. Correspondingly, there is a rapid increase in shear rate. It is at this location that polymers which exhibit very high viscosities (above 10 Pa s at shear rate ~800 s^{-1}) seem to block the channel. The pressure and shear rate comparison are illustrated in Figures 6 and 7 respectively, showing that maximum pressure exists at the entry to the die, with shear rates that increase as the rotation rate is increased from 5000 to 10,000 rpm.

Having gained some insight into the flow behavior from the CFD analysis, experimental trials were then conducted for model validation. During RJS, polymer systems that blocked the die channel or flowed through but created droplets on the collector were marked as failures, as continuous, bead-free fibers were not produced. These unsuccessful spinning experiments would form the basis of the lower and upper viscosity limits of the trial. Following this, pressure calculations were made for each respective trial and compared against the viscosity of the polymer at shear rates (~800 s^{-1}) that would be experienced during spinning. The data as shown in Figure 9 represent the outcome of the spinning limitation study that we set out to do. In this graph, we showed that polymers with a viscosity below ~1 Pa s did not produce fibers due to insufficient chain entanglement in either polymer melt or solution. On the other
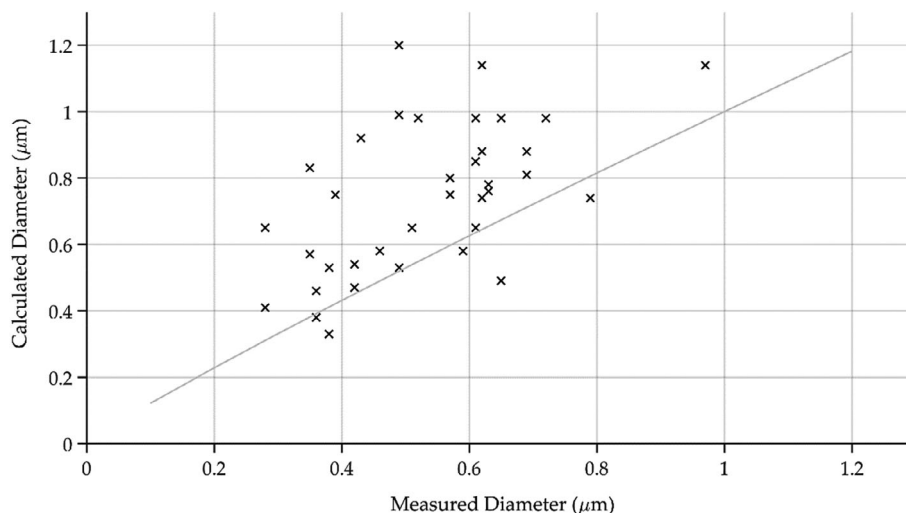
Figure 10. Fiber diameter comparison between Mellado *et al.*[39] model (line) and measured fiber diameters. The variation in fiber diameter signifies a less than perfect fit. Alternative tests in melt spinning showed even greater disparity, confirming the need for additional parameters to be considered.

hand, for polymers with viscosities exceeding ~10 Pa s, we experienced blockage in the spinneret as discussed.

It is expected that the inclusion of shear thinning effects will not change the main conclusions of this article. We can perform a simple thought experiment in support of this argument. In the device, the flow is practically unidirectional and the Reynolds number is low. A force balance between the pressure forces driving the flow and the resistive viscous forces requires $\Delta p \propto \eta \dot{\gamma}$, where $\dot{\gamma}$ here is the shear rate at the wall and where the shear rate is maximum. This equation tells us that for a given rotational velocity (and thus for a fixed Δp), the maximum shear rate obtained with a shear thinning fluid, $\dot{\gamma}_s$, is related to the maximum shear rate with the corresponding Newtonian fluid, $\dot{\gamma}_n$, by the formula $\dot{\gamma}_s = \dot{\gamma}_n \frac{\eta_n}{\eta_s}$. Using eq. (3), it can be easily shown that for polymers with strong shear-thinning behavior $\dot{\gamma}_s \approx \left(\frac{\eta_n}{\eta_0} k^n \dot{\gamma}_n \right)^{\frac{1}{1-n}}$ reduces to $\dot{\gamma}_s \approx (k^n \dot{\gamma}_n)^{\frac{1}{1-n}}$ for $\eta_n = \eta_0$. Using the data in Table III for a PE melt at $M_w = 40{,}000$ g mol^{-1} yields $\dot{\gamma}_s \tilde{0}.1(\dot{\gamma}_n)^{1.92}$, which predicts a shift to the right of the simulation curves in Figure 8 by one-order of magnitude, from $\dot{\gamma}_s \sim 100$ s^{-1} to about $\dot{\gamma}_s \sim 1000$ s^{-1}. However, we know that PE with $M_w = 40{,}000$ g mol^{-1} does not produce fibers, and thus the index n must be significantly smaller than 0.48 for polymers that do produce fibers. Even taking n between 0.1 and 0.3 to evaluate strong shear thinning effects, we obtain a maximum shear rate in the non-Newtonian case between 165 and 691 s^{-1}, which is still within the range of shear rates reported in Figure 8 and simulated assuming Newtonian behavior. The use of simulation data in evaluating the measured viscosity as 800 s^{-1}, as done in Figure 9, is thus reasonable. For our polymer producing fibers, we know that $\eta \le 10$ Pa s, thus $n \ll 1$. Hence, the use of simulation data to extract the data points in Figure 9 is justified.

In future, it is, however, worth considering the evaporation mechanism of polymer solutions during spinning. Polymer solutions contain a solvent which is required to evaporate during spinning to produce a fiber. In case of a too volatile solvent, the fast-moving air in the spinning chamber will start to solidify the polymer leaving the tip of the die before it gets a chance to extrude, causing a blockage. Conversely, if the solvent has a too low volatility and does not readily evaporate through exposure to fast flowing air, the polymer fiber will be heavily beaded upon collection. This could therefore lead to solutions with shear viscosities outside the processing window that has been suggested here, for example, solutions based on rapidly evaporating solvents could have a shear viscosity below 1 Pa s and still produce fibers.

Die entry pressures increase through a change in geometry, rotational velocity, or the addition of an external pressure coupling, such as in the pressurized gyration process.[47–49] A combination of any of these modifications could potentially widen the overall range of fiber producing viscosities. As shown in our data, the pressure at which a polymer starts to extrude from a 0.16 μm diameter die exceeds 400 kPa.

Further research into the model could include variations of die geometries and die channel lengths which would allow for much higher pressures, and therefore viscosities, to produce fibers.

Reducing the channel length will reduce the pressure required to extrude the polymer in addition to a variation in the radius of the spinneret, which would increase die entry pressure for larger radius geometries. Directions for further research could also include reduction and recovery of solvents in solution spinning or spinning of higher molecular weight polymer melts, allowing for enhanced mechanical performance over existing polymer melt options.

CONCLUSIONS

RJS was investigated for the analysis of rheological material limitations. Using CFD and physical spinning trials, a viscosity range for spinning was determined. RJS was shown to produce fibers that were continuous and bead-free in the case of Newtonian solutions with viscosities of 1–10 Pa s. In evaluating successful and unsuccessful experimental spinning outcomes, we have produced a region of spinnability that has not yet been reported. From this region of spinnability, a pressure and viscosity range that shows successful fiber production was identified. It was shown that Newtonian flow behavior is most suited to RJS; however, high shear rates of around 800 s^{-1} are present during processing, which allows for shear thinning non-Newtonian fluids with low enough viscosities to potentially be used at these shear rates. Further considerations are necessary to evaluate the impact of solution evaporation rates, die geometry, and polymer melt temperatures on the production of fibers by RJS.

REFERENCES

1. Yarin, A. L.; Pourdeyhimi, B.; Ramakrishna, S. Fundamentals and Applications of Micro and Nanofibers; Cambridge University Press: Cambridge, UK, **2014**.

2. Rogalski, J. J.; Bastiaansen, C. W. M.; Peijs, T. *Nanocomposites.* **2017**, *3*, 97.

3. Yao, J.; Bastiaansen, C. W. M.; Peijs, T. *Fibers.* **2014**, *2*, 158.

4. Bognitzki, M.; Czado, W.; Frese, T.; Schaper, A.; Hellwig, M.; Steinhart, M.; Greiner, A.; Wendorff, J. H. *Adv. Mater.* **2001**, *13*, 70.

5. Peijs, T. Comprehensive Composite Materials II. Vol. *6*; Elsevier: Oxford, UK, **2018**. p. 162 Chapter 6.7.

6. Ellison, C. J.; Phatak, A.; Giles, D. W.; Macosko, C. W.; Bates, F. S. *Polymer.* **2007**, *48*, 3306.

7. Moreno, M. J.; Ajji, A.; Mohebbi-Kalhori, D.; Rukhlova, M.; Hadjizadeh, A.; Bureau, M. N. *J. Biomed. Mater. Res. B Appl. Biomater.* **2011**, *97*, 201.

8. Wang, X.; Um, I. C.; Fang, D.; Okamoto, A.; Hsiao, B. S.; Chu, B. *Polymer.* **2005**, *46*, 4853.

9. Fedorova, N.; Pourdeyhimi, B. *J. Appl. Polym. Sci.* **2007**, *104*, 3434.

10. Anantharamaiah, N.; Verenich, S.; Pourdeyhimi, B. *J. Eng. Fibers Fabr.* **2016**, *3*, 1.

11. Feng, L.; Li, S.; Li, H.; Zhai, J.; Song, Y.; Jiang, L.; Zhu, D. *Angew. Chem. Int. Ed. Engl.* **2002**, *41*, 1221.

12. Schönenberger, C.; Van der Zande, B. M. I.; Fokkink, L. G. J.; Henny, M.; Schmid, C.; Krüger, M.; Bachtold, A.; Huber, R.; Birk, H.; Staufer, U. *J. Phys. Chem. B.* **1997**, *101*, 5497.

13. Wang, J.; Zhang, D. *Adv. Polym. Technol.* **2013**, *32*, E323.

14. Ondarçuhu, T.; Joachim, C. *Europhys. Lett.* **1998**, *42*, 215.

15. Ma, P. X.; Zhang, R. *J. Biomed. Mater. Res.* **1999**, *46*, 60.

16. Hartgerink, J. D.; Beniash, E.; Stupp, S. I. *Science.* **2001**, *294*, 1684.

17. Whitesides, G. M.; Grzybowski, B. *Science.* **2002**, *295*, 2418.

18. Nayak, R.; Padhye, R.; Kyratzis, I. L.; Truong, Y. B.; Arnold, L. *Text. Res. J.* **2011**, *82*, 129.

19. Luo, C. J.; Stoyanov, S. D.; Stride, E. P. J.; Pelan, E. G.; Edirisinghe, M. J. *Chem. Soc. Rev.* **2012**, *41*, 4708.

20. Shanmuganathan, K.; Fang, Y.; Chou, D. Y.; Sparks, S.; Hibbert, J.; Ellison, C. J. *ACS Macro Lett.* **2012**, *1*, 960.

21. O'Haire, T.; Rigout, M. L. A.; Russell, S. J.; Carr, C. M. *J. Thermoplast. Compos. Mater.* **2014**, *27*, 205.

22. Raghavan, B.; Soto, H.; Lozano, K. *J. Eng. Fibers Fabr.* **2013**, *8*, 52.

23. Sweetser, D. M.; Zander, N. E. ARL-TN-0619. In: Army Research Laboratory Aberdeen Proving Ground MD; **2014**.

24. Zander, N. E. *J. Appl. Polym. Sci.* **2015**, *132*, 9.

25. Chen, H.; Xu, H.; Sun, J.; Liu, C.; Yang, B. *Micro Nano Lett.* **2015**, *10*, 81.

26. Rogalski, J.; Bastiaansen, C.; Peijs, T. *Fibers.* **2018**, *6*, 37.

27. Padron, S.; Patlan, R.; Gutierrez, J.; Santos, N.; Eubanks, T.; Lozano, K. *J. Appl. Polym. Sci.* **2012**, *125*, 3610.

28. Sarkar, K.; Gomez, C.; Zambrano, S.; Ramirez, M.; de Hoyos, E.; Vasquez, H.; Lozano, K. *Mater. Today.* **2010**, *13*, 12.

29. Amalorpava Mary, L.; Senthilram, T.; Suganya, S.; Nagarajan, L.; Venugopal, J.; Ramakrishna, S.; Giri Dev, V. R. *eXPRESS Polym. Lett.* **2013**, *7*, 238.

30. Ren, L.; Pandit, V.; Elkin, J.; Denman, T.; Cooper, J. A.; Kotha, S. P. *Nanoscale.* **2013**, *5*, 2337.

31. Agubra, V. A.; De La Garza, D.; Gallegos, L.; Alcoutlabi, M. *J. Appl. Polym. Sci.* **2016**, *133*, 42847.

32. Zimm, B. H. *J. Chem. Phys.* **1956**, *24*, 269.

33. Rouse, P. E. *J. Chem. Phys.* **1953**, *21*, 1272.

34. Teraoka, I. Polymer Solutions: An Introduction to Physical Properties; John Wiley & Sons: New York, USA, **2002**. p. 64 Chapter 1.

35. Lu, Y.; Li, Y.; Zhang, S.; Xu, G.; Fu, K.; Lee, H.; Zhang, X. *Eur. Polym. J.* **2013**, *49*, 3834.

36. Vega, J. F.; Rastogi, S.; Peters, G. W. M.; Meijer, H. E. H. *J. Rheol.* **2004**, *48*, 663.

37. Yan, D.; Wang, W. J.; Zhu, S. *Polymer.* **1999**, *40*, 1737.

38. Vega, J. F.; Fernández, M.; Santamaría, A.; Muñoz-Escalona, A.; Lafuente, P. *Macromol. Chem. Phys.* **1999**, *200*, 2257.

39. Mellado, P.; McIlwee, H. A.; Badrossamay, M. R.; Goss, J. A.; Mahadevan, L.; Kit Parker, K. *Appl. Phys. Lett.* **2011**, *99*, 203107.

40. Padron, S.; Caruntu, D.I.; Lozano, K. In ASME 2011 International Mechanical Engineering Congress and Exposition; Vol. 7 Pts A and B; American Society of Mechanical Engineers Digital Collection 2011; p. 821.

41. Padron, S.; Caruntu, D.I.; Lozano, K., In ASME 2012 International Mechanical Engineering Congress and Exposition; Vol. 4 Pts A and B; American Society of Mechanical Engineers Digital Collection **2012**; p 889.

42. Taghavi, S. M.; Larson, R. G. *Phys. Rev. E Stat. Nonlin. Soft Matter Phys.* **2014**, *89*, 023011.

43. Noroozi, S.; Alamdari, H.; Arne, W.; Larson, R. G.; Taghavi, S. M. *J. Fluid Mech.* **2017**, *822*, 202.

44. Divvela, M. J.; Ruo, A.-C.; Zhmayev, Y.; Joo, Y. L. *J. Non-Newtonian Fluid Mech.* **2017**, *247*, 62.

45. Osswald, T.; Rudolph, N. Polymer Rheology Fundamentals and Applications; Carl Hanser Verlag GmbH & Co. KG: Munich, Germany, **2014**.

46. Golecki, H. M.; Yuan, H.; Glavin, C.; Potter, B.; Badrossamay, M. R.; Goss, J. A.; Phillips, M. D.; Parker, K. K. *Langmuir.* **2014**, *30*, 13369.

47. Mahalingam, S.; Edirisinghe, M. *Macromol. Rapid Commun.* **2013**, *34*, 1134.

48. Mahalingam, S.; Pierin, G.; Colombo, P.; Edirisinghe, M. *Ceram. Int.* **2015**, *41*, 6067.

49. Mahalingam, S.; Ren, G.; Edirisinghe, M. *Carbohydr. Polym.* **2014**, *114*, 279.